

300 **Elemental abundances of major elements in the solar wind as measured in**
301 **Genesis targets and implications on solar wind fractionation**

302

303 Veronika S. Heber^{1,2}, Kevin D. McKeegan¹, Robert C. J. Steele^{1,3}, Amy J. G.
304 Jurewicz⁴, Karen D. Rieck^{4,5}, Yunbin Guan⁶, Rainer Wieler^{7,6,*}, Donald S.
305 Burnett⁶

306 Submitted to *Astrophysical Journal*, September 8, 2020; revision submitted Oct. 27, 2020

307 Short title: Solar Wind Element Abundances from Genesis Targets

308 -----

309 1. Department of Earth, Space, and Planetary Sciences, UCLA, 595 Charles Young Drive East, Geology
310 Building, Los Angeles, California 90095-1567, United States

311 2. Paul Scherrer Institut, Division for Radiation Safety and Security, 5232 Villigen PSI, Switzerland

312 3. School of Earth & Environmental Sciences, University of St. Andrews, St. Andrews KY16 9AJ, UK

313 4. Center for Meteorite Studies, Arizona State University, m/c 6004, Tempe, Arizona 85287, USA

314 5. New Mexico Consortium, 4200 W. Jemez Rd, Suite 200, Los Alamos, NM 87544, USA

315 6. California Institute of Technology, Division of Geological and Planetary Sciences, Pasadena CA
316 91125, USA.

317 7. Institute of Geochemistry and Petrology, Department of Earth Sciences, ETH Zürich, Clausiusstrasse
318 25, 8092 Zürich, Switzerland

319 * Corresponding author: wiel@erdw.ethz.ch

320

321 Orchid:

322 KDMK: 0000-0002-1827-729X

323 RCJS: 0000-0003-1406-6855

324 AJGJ: 0000-0002-3282-5782

325 YG: 0000-0002-7636-3735

326 KDR: 0000-0002-7427-9134

327 RW: 0000-0001-5666-7494

328 DSB: 0000-0001-9521-8675

329
330
331
332
333
334
335
336
337
338
339
340
341
342
343
344
345
346
347
348
349

Abstract

We present elemental abundance data of C, N, O, Na, Mg, Al, Ca, and Cr in Genesis silicon targets. For Na, Mg, Al, and Ca, data from three different SW regimes are also presented. Data were obtained by backside depth profiling using Secondary Ion Mass Spectrometry. The accuracy of these measurements exceeds those obtained by in-situ observations; therefore the Genesis data provide new insights into elemental fractionation between Sun and solar wind, including differences between solar wind regimes. We integrate previously published noble gas and hydrogen elemental abundances from Genesis targets, as well as preliminary values for K and Fe. The abundances of the solar wind elements measured display the well-known fractionation pattern that correlates with each element's First Ionization Potential (FIP). When normalized either to spectroscopic photospheric solar abundances or to those derived from CI-chondritic meteorites, the fractionation factors of low-FIP elements (K, Na, Al, Ca, Cr, Mg, Fe) are essentially identical within uncertainties, but the data are equally consistent with an increasing fractionation with decreasing FIP. The elements with higher FIPs between ~ 11 and ~ 16 eV (C, N, O, H, Ar, Kr, Xe) display a relatively well-defined trend of increasing fractionation with decreasing FIP, if normalized to modern 3D photospheric model abundances. Among the three Genesis regimes, the Fast SW displays the least elemental fractionation for almost all elements (including the noble gases) but differences are modest: for low-FIP elements the precisely measured Fast-Slow SW variations are less than 3%.

1. INTRODUCTION

350
351
352
353
354
355
356
357
358

359
360
361
362
363
364
365
366
367
368

369
370
371
372
373
374

NASA's Genesis spacecraft collected solar wind (SW) ions for laboratory analysis with the goals to obtain high precision isotopic and elemental abundances of solar matter. In order to constrain the amounts of fractionation between the SW and the photosphere, besides the Bulk SW the mission sampled three different SW regimes: interstream (Slow), coronal hole (Fast), and coronal mass ejections (CME) (Burnett and team 2011; Burnett 2013; Reisenfeld et al. 2013; Neugebauer et al. 2003). To meet the Mission goals, the accuracy of the measurement is required to meet the needs of planetary science.

So far, these goals have been fully or largely achieved for the noble gases (e. g. Grimberg et al. 2006; Heber et al. 2009; Meshik et al. 2007; Meshik et al. 2014; Meshik et al. 2020; Crowther & Gilmour 2013; Pepin et al. 2012; Vogel et al. 2011; Vogel et al. 2019), with only Kr and Xe isotopic composition data from regime targets missing. Isotopic data are also available for O and N in Bulk SW, the two highest priorities of Genesis (McKeegan et al. 2011; Marty et al. 2010; Marty et al. 2011, Huss et al. 2012) and Mg (Jurewicz et al., 2020). Hydrogen fluences in Bulk SW and regime targets were published by Huss et al. (2020). For a number of other elements important for cosmochemistry, elemental abundances in Bulk SW targets have been published in preliminary form (Heber et al. 2013; Heber et al. 2014b,c; Rieck 2015; Rieck et al. 2016; Burnett et al. 2017).

For the first time, this work presents comprehensive elemental abundance data for four cosmochemically important elements in Genesis Bulk SW and regime targets: Na, Mg, Al, Ca. We also present our final abundance data of C, N, O, and Cr for Bulk SW targets. We put these data into perspective by calculating the extent of elemental fractionation between Sun and solar wind, with a special emphasis on the elements for which solar wind abundances in the different regimes are available. All data were obtained by Secondary Ion Mass Spectrometry (SIMS)

375 using backside depth profiling. Some details of this technique will be briefly explained in the
376 next section, for a full description see Heber et al. (2014a).

377 It is well known that elemental fractionation upon solar wind formation correlates with the First
378 Ionization Potential (FIP) of the elements (e.g., Pilleri et al., 2015). Elements with low FIP
379 (below some 9-10 eV) are overabundant relative to O in the solar wind by a factor of a few.
380 The elements measured in this work for which regime data are available are all low-FIP
381 elements, ranging from 5.14 eV (Na) to 7.65 eV (Mg), whereas C, N, and O for which we
382 present Bulk solar wind fluences have high FIPs, between 11.3 and 14.5 eV. For a better
383 understanding of the underlying fractionation mechanisms, we therefore also consider in the
384 discussion the fluence data for high-FIP elements for which Genesis regime data are available,
385 in particular noble gases (Heber et al. 2009; Heber et al. 2012; Vogel et al. 2019) and hydrogen
386 (Huss et al. 2020). We also include data for K (Rieck 2015; Rieck et al. 2016) and Fe (Burnett
387 et al. 2017) in Bulk SW targets.

388 In section 2, we will discuss the analytical technique of analyzing concentrations of elements
389 implanted by the solar wind in Genesis targets. In section 3 we will present the main
390 experimental results and in section 4 we will discuss these data in terms of solar wind
391 fractionation effects as well as solar elemental abundances.

392

393

2. EXPERIMENTAL

394

395 Fluences of implanted solar wind elements were analyzed by backside depth profiling using
396 SIMS. This method is widely employed in the semiconductor industry to analyze depth
397 distributions of dopant elements (e. g. Zinner 1983). In this work, SW-bearing silicon wafers
398 of 0.55-0.7 mm thickness were glued upside down onto a Si substrate and then thinned

424 Bulk SW targets during the entire ~2.3 year duration of the Genesis collection period, whereas,
425 in addition to Bulk SW, Na, Mg, Al, and Ca were also measured in regime samples. The "Fast"
426 and "Slow" regimes were sampled for slightly more than 300 days each, CMEs for ~190 days.
427 Reisenfeld et al. (2007, 2013) and Neugebauer et al. (2003) give details about the Genesis
428 regime selection and SW properties during the different regimes. There is an overlap in Fast
429 SW and Slow SW speed intervals as defined by the regime selection algorithm, essentially in
430 the range between ~400 – 540 km/s, while the CME targets also sampled at least ~25% of non-
431 CME SW (Reisenfeld et al. 2013).

432

433

2.2. SIMS analytical techniques

434

435

436

437

438

439

440

441

442

443

444

445

446

2. 3. Sample analysis

447

448

The thinned Si solar wind collectors were sputtered from the backside with minor modifications from traditional backside-sputtering techniques used by the semiconductor industry (see Heber

449 et al. 2014a for details). In most cases only one element of interest was analyzed per session, to
450 maximize the data coverage. Due to their similar masses, Mg and Na require lower waiting
451 times upon peak switching and thus these two elements were analyzed in the same session.
452 Details on data reduction techniques and fluence calibrations are given by Heber et al. (2014a)
453 and summarized in Appendices A1 and A2.

454

455 2.4. Uncertainties

456 Stated 1σ uncertainties of the mean solar wind fluence of elements given in Table 1 include the
457 standard deviation of all fluence measurements and the mean uncertainties of all relative
458 sensitivity factors (RSF) and sputtering rates (S) (Appendix, section A2, Table 4). The total
459 uncertainty of the mean Bulk solar wind fluence includes the uncertainty of the absolute
460 calibration and 10% for N, and Al which are not calibrated.

461

462 3. RESULTS

463 The mean solar wind fluences for each element (and each regime, when available) are
464 given in Table 1. The table also shows noble gas fluences for Bulk SW and Genesis regimes,
465 slightly updated from those given by Heber et al. (2009) and Vogel et al. (2019) with details
466 explained in the Appendix (section A4). The H fluences are those from Huss et al. (2020)
467 measured by SIMS in Genesis targets. Uncertainties (1σ) for Bulk fluences include
468 uncertainties of standards (Heber et al. 2014a; Vogel et al. 2019; Huss et al. 2020). Uncertainties
469 of regime data do not include the systematic uncertainties of the standards, since these cancel
470 when comparing differences in fluences and element ratios in different regimes. The complete
471 data collected during this study is given in Table 4 in the Appendix.

472 The exposure-duration-weighted sum of regime fluences should be the same as the Bulk
473 fluence. The calculated Bulk fluences agree within uncertainties with the values measured in
474 Bulk SW targets: summed regime fluences amount to 97%, 97%, 93%, and 98% of the Bulk
475 collector values for Na, Mg, Al, Ca, respectively. For comparison, the weighted total regime
476 fluence of H measured by Huss et al. (2020) amounted to 99% of their Bulk SW target value,
477 if the slightly lower total exposure durations of the three regime arrays is taken into account.

478

479

4. Discussion

480

481

4.1. Low-FIP elements

482

483 Figure 2 shows the ratios of the relative fluences (element/Mg) measured in Genesis Bulk SW
484 (Fig. 2a) and regime targets (Fig. 2b) after normalization to the respective solar abundance
485 ratios (Table 7 in the Appendix). The Bulk SW data for K and Fe in silicon (marked by asterisks
486 in Figure 2a) are the preliminary fluences from Rieck (2015), Rieck et al. (2016) and Burnett
487 et al. (2017). If SW had the composition of the solar photosphere, the ordinate value in Figure
488 2 would be 1 for all elements. The Bulk SW shows a fractionation of elemental abundances
489 correlating with FIP, as previously observed by spacecraft (e. g., Geiss, 1982; Bochsler, 2009).
490 However, the better accuracy and element coverage of Genesis data compared to in-situ
491 measurements allows further insights into this FIP-related fractionation. The low-FIP elements
492 (Fig. 2a) are consistent with a flat pattern, at least below 7 eV, as many pre-Genesis studies
493 suggested. This consistency would make these SW data easier to apply to cosmochemistry, as
494 they would suggest that low-FIP elements are unfractionated relative to each other and hence
495 their solar wind abundance ratios equal photospheric ratios. However, Fig. 2a is also consistent
496 with a monotonic increase of the low-FIP elements with decreasing FIP, which could be viewed

497 as a trend continuing that of the high-FIP elements between Ar and C discussed below. The Na
498 abundance given here is about 20% higher than that of Burnett et al. (2017). Na fluences
499 derived from backside depth profiling of diamond-like-C collectors are roughly a factor of 2
500 lower than ours, which are based on Si collectors (Rieck, 2015; Rieck et al., 2016). Jurewicz et
501 al. (2019) propose that diffusion of surface contamination Na might have enhanced fluences
502 from Si collectors. Since the amounts of surface contamination is highly variable, the Na
503 fluences from Si should show significant scatter; however replicate analyses of Bulk and regime
504 samples agree to within 2 – 11% (Table 4, Appendix). More analyses are required to resolve
505 this important discrepancy. A ~20% lower fractionation of K compared to that of Na, if real,
506 would be surprising although within 2σ both values still overlap.

507 Inefficient Coulomb drag (Bodmer and Bochsler, 2000) would not predict such a difference in
508 fractionation between two elements of almost equal mass (K and Ca). These elements are
509 expected to have a similar charge state distribution; moreover the difference would also run
510 opposite to the possible increase of fractionation with decreasing FIP mentioned above. The
511 final Genesis-derived abundance of K will be important in this comparison.

512 The FIP fractionation pattern predicted by the model of Laming et al. (2017, 2019) is in
513 reasonable agreement with the low-FIP element data in Fig. 2a. This model explains FIP
514 fractionation by the ponderomotive force in the chromosphere. Conservation of the adiabatic
515 invariant during acceleration away from the photosphere is invoked to account for isotope
516 fractionation.

517 Figure 3 shows a FIP trend of solar wind element/Mg ratios normalized to the values in CI
518 carbonaceous chondrites instead of photospheric spectroscopic abundances. Elemental
519 abundances in CI chondrites (e. g. Lodders, 2020) are often used as a surrogate of solar
520 abundances for most elements, because of the overall agreement between CI and photospheric
521 values derived by spectroscopy when available. On the other hand, solar abundances should be

522 based on data from the Sun: to clarify the validity of CI abundances as proxy for solar values
523 is one of the ultimate goals of Genesis. At this point, we note that the apparent fractionation
524 factors element/Mg in Fig. 3 show a slightly smaller spread than those in Fig. 2a, with all ratios
525 agreeing within better than 25% with CI values.

526 Figure 2b shows the fractionation patterns of the different Genesis regime targets as function
527 of FIP, again with Mg as normalizing element. In-situ data generally reveal that the
528 fractionation between low-FIP and high-FIP elements is less for Fast than Slow SW (e. g. von
529 Steiger et al. 2000; Bochsler 2009). This is also observed in Fig. 2b, i.e. the Fast solar wind
530 fractionation factors are closer to 1 (lower for low-FIP elements and higher for high-FIP
531 elements). Most importantly, for low-FIP elements, differences in normalized element/Mg
532 ratios are small, not more than 10% between CME and Fast SW and even less between Slow
533 SW and Fast SW. These differences are significant beyond the 1 sigma level only for Ca and
534 (marginally) Al in CME targets. In particular, the Na/Mg ratio shows the smallest spread among
535 the low-FIP elements, perhaps contrary to expectations, given that Na appears to show the
536 strongest fractionation in the Bulk SW among all elements shown in Fig. 2a.

537 Even given the overlap in SW speeds actually sampled by the Fast- and Slow-SW regimes, the
538 close similarity of the low-FIP fractionation patterns in Figure 2b is new and potentially
539 important. This has not been recognized by previous studies of solar wind composition
540 primarily because of the high precision possible in inter-regime comparisons of element ratios
541 in our data (Table 2). For these comparisons, the major source of errors in the fractionation
542 factor do not enter: from implant standard calibrations and from the spectroscopic photospheric
543 abundances. The analytical precision of the ratios in Table 2 is 1.6 to 4.6%. As noted above,
544 significant inter-regime differences (4.8-11.2%) are observed, but the important point is that
545 these are small, especially between Fast and Slow regimes. The Fast and Slow solar wind form
546 by different mechanisms in different solar environments (e.g. Neugebauer and von Steiger

2001; Laming et al. 2017). Consequently, it seems unlikely that fractionations among low-FIP elements would be the *same* for both Fast and Slow as shown in Table 2. This is possibly an indirect, but potentially strong, argument that there are no fractionations among the low-FIP elements as a set (i.e. a flat pattern on Figure 1). There, of course, is still the larger fractionation between high- and low-FIPs which is a separate issue. Non-fractionation among low-FIP elements might only hold below about 7 eV. Pilleri et al. (2015) propose, based on processing ACE-SWICS data for the Genesis period, that there is non-FIP mass dependent fractionation between Mg and Fe. As discussed in the Appendix (Section A5), our result is fully compatible with previous SW composition data sets. The widely-recognized smaller fractionation of Fast SW is primarily a smaller difference between low-FIP and high-FIP elements taken as groups, specifically between low-FIP elements and O.

Figure 4 shows flux ratios in Genesis regimes over those in Bulk SW. This format is independent of assumed solar compositions as well as of absolute calibration uncertainties when inter-regime comparisons are being made. First we note that the observation based on noble gases (Vogel et al. 2019) that fluxes increase in the order Fast – Slow – CME also holds for the low-FIP elements. Furthermore, three different groupings are observed: i) the low-FIP elements show substantially different fluxes in the different regimes, ii) fluxes for H, Kr, and Ar are similar within 20% in all three regimes, and iii) He and Ne again show large differences. There also appears to be a crossover pattern, in that the flux differences between Fast SW and CMEs first seem to decrease with increasing FIP, while they clearly increase again for the two highest FIP elements Ne and He.

568

569

4.2 High-FIP elements

570 In Fig. 2a, the data for C, N, O (and H) for Bulk SW fit into the noble gas pattern already
571 discussed by Vogel et al. (2019). For both Bulk and regime SW samples these high-FIP
572 elements display the above-mentioned trend of increasing normalized abundances with
573 decreasing FIP in the 15-11 eV region between Ar and C (see also Meshik et al., 2020).
574 Abundance ratios Xe/Kr and Xe/Ar higher in the solar wind than solar were already observed
575 based on lunar regolith data (Wieler and Baur 1995; Wieler et al. 1996). Geiss and Bochsler
576 (1985) proposed to explain this enhancement of Xe to be due to the fact that in the solar wind
577 source region Xe has a relatively low first ionization time (FIT), the characteristic time for an
578 element to undergo its first ionization in the chromosphere, a parameter closely related to FIP.
579 Xenon indeed has the lowest FIT of all elements between 15-11 eV shown in Fig. 2a. However,
580 otherwise there is no conspicuous dependence of the fractionation factors of these elements on
581 FIT, indicating that FIT is not the most relevant parameter governing the SW abundance pattern
582 in the high-FIP region below Ne.

583 The position of the CNO points in Fig. 2a is also relevant for the discussion of solar elemental
584 abundances of these three elements (e. g., von Steiger and Zurbuchen 2016; Serenelli et al.
585 2016). Note that the position of the Kr and Xe points relative to that of H is well constrained
586 since i) Kr and Xe abundances in the solar wind are well known thanks to the precise noble gas
587 data (including He) provided by Genesis and the accurate He abundance provided by
588 helioseismology and ii) solar Kr and, to a lesser extent, Xe abundances can be derived with
589 high confidence, Kr by interpolating meteoritic abundances of neighboring elements, Xe from
590 nucleosynthesis theory (cf. Table 7 (Appendix) and Meshik et al. 2020). The fact that the CNO
591 points in Fig. 2a display the same trend as H, Kr, and Xe is, thus, an argument in favor of the
592 solar abundances of CNO used here, which are those given by Asplund et al. (2009). This
593 speaks against the suggestion by Laming et al. (2017) that the difference between their modeled

594 fractionations and the measured data in the high-FIP region may indicate an underestimation of
595 the solar O and N abundances by Asplund et al. (2009).

596 The high-FIP elements show systematic differences in the different regimes (Fig. 2b). Their
597 abundances relative to Mg are more fractionated in CME and Slow SW than in the Fast SW (i.
598 e., Fast SW data points plot closest to the 1 : 1 line). Relative differences are modest, yet tend
599 to be somewhat larger than those for the low-FIP elements (e. g. ~28% for Ar/Mg in Fast versus
600 Slow wind), The only exception to this is He where the CME point falls marginally above that
601 of Fast SW. In terms of He/H the CME ratio is about 25 - 30%% higher than Slow or Fast (Huss
602 et al., 2020, Figure 18). Figure 4 shows that relative fluxes of Ne and especially He increase
603 markedly in CMEs (by about 16% in the case of He), which is compensated by a roughly
604 parallel decrease of the relative fluxes of these two elements in Fast and Slow SW (see also
605 Vogel et al., 2019). High He/H is observed in *some* CME events (Borrini et al., 1982). It is also
606 worth noting that the Genesis „CME“ sample is basically all ions that were not clearly Fast or
607 Slow SW and could contain several different sources of high He solar wind. High He/H was
608 one, but only one, of the factors that triggered the deployment of the Genesis CME array.

609

610 Also notable on the high-FIP side of Fig. 4 are two further observations. First, in all three
611 regimes the Kr flux closely follows H which has a very similar FIP. Second, whereas the Slow
612 regime shows a monotonic decrease with FIP from Mg to He, in the Fast SW, Xe, H, and Kr
613 increase markedly relative to Mg in the Fast SW. These observations further indicate that the
614 fractionation of the high-FIP elements in the solar wind is governed by more than the first
615 ionization potential.

616

617 4.3 Comparing Genesis-derived elemental abundances with in-situ data

618 Reames (2019) reviews element abundances measured in solar energetic particles (SEPs).
619 Large (gradual) SEP events show an abundance pattern similar to that of the solar wind, with
620 low-FIP element/O ratios being enhanced by factors of 2 – 3 relative to photospheric
621 abundances. SEP abundances given by Reames (2019) are compared with the values for Bulk
622 SW Genesis targets in Fig. 5, where we use Mg and O as reference elements for the low-FIP
623 (upper panel) and high-FIP (lower panel) elements, respectively. The agreement between SEP
624 and Genesis-derived SW values is remarkably good for all low-FIP elements shown. A
625 similarly good agreement had also been noted by Reames (2019) between SEPs and in-situ
626 derived SW abundances (Bochsler 2009), indicating a common lack of fractionation among
627 low-FIP elements relative to the photosphere in the solar wind and in the higher-energy gradual
628 SEPs. Particularly remarkable is the close agreement in Mg and Fe, which have similar FIPs.
629 The high-FIP region (Fig 5b) shows less good agreement between SEP and SW abundances.
630 Most remarkably, C is enhanced in the SW by ~30% relative to O in SEPs, while N - as well
631 as Ar, Ne, and He - are depleted by 20-30% in the SW relative to SEPs. A similarly high C/O
632 ratio in the (Slow) in-situ-SW relative to the SEP ratio was also observed by Reames (2019)
633 who also noted even somewhat larger differences for S and P, two elements with a similar FIP
634 as C. He pointed out that this indicates that the SEPs are not just accelerated solar wind but are
635 an independent sample of the solar corona, and noted that the transition from "low-FIP" to
636 "high-FIP" occurs at a lower value for SEPs than for the Slow solar wind. The Genesis C
637 abundance confirms this observation also for the Bulk solar wind.

638

639 Pilleri et al. (2015) report mean abundance ratios (element/Mg) for 8 elements measured by the
640 Solar Wind Ion Composition Spectrometer (SWICS) on the Advanced Composition Explorer
641 (ACE) during the same time window as Genesis collection. In the upper part of Table 3 these
642 ratios are compared with the data of this work for the five element pairs for which Bulk SW

643 data are available in both studies. Only for Ne/Mg and He/Mg regime data are available in both
644 studies. In the lower part of the table we report these ratios normalized to the respective Bulk
645 SW values. All five elemental abundance ratios from both studies agree within their formal
646 uncertainties, for O/Mg and Ne/Mg the agreement is actually very satisfying.

647

648

5. Conclusions

649 This paper presents data on elemental abundances in the solar wind for elements with a wide
650 range in first ionization potentials obtained by laboratory analyses on Genesis targets. Such data
651 are of higher precision than can be reached by in-situ observations and can be used to support
652 studies of SW fractionation processes and possibly solar abundances of key elements more
653 quantitatively than measurements obtained by space-borne instruments. All elements discussed
654 here (C, N, O, Na, Mg, Al, Ca, Cr, H, K, Fe and the noble gases) are also of great interest in
655 planetary sciences. In some cases, the data presented here approach the accuracy required to
656 test the extent to which elemental abundances of CI chondrites approach solar abundances. The
657 Genesis data are consistent with the view that CI data represent the solar abundances of the
658 low-FIP elements studied here as well as spectroscopically obtained values. Intermediate to
659 high-FIP elements between 10 – 16 eV (C, N, O, H, Kr, Xe, Ar) display a well-defined trend
660 of increasing solar wind abundances with decreasing FIP if normalized to 3D-model-derived
661 solar values. In particular Kr and Xe, whose solar abundances are independently known and
662 whose solar wind abundances are well anchored to H via the well-known abundances of He in
663 the outer convective zone of the Sun as well as in the solar wind speak in favor of the 3D-model
664 values (Asplund et al., 2009). Where Genesis data are available for the solar wind regimes, the
665 Fast regime is always less fractionated than Slow and CME solar wind, as expected, although
666 the differences are modest. For low FIP elements the inter-regime variations are precisely
667 measured (Table 2), the Fast-Slow SW differences are less than 3%. Abundances of low-FIP

668 elements measured in gradual Solar Energetic Particle events (Reames, 2019) agree well with
669 SW abundances obtained here, whereas the high C/O ratio in the SW relative to the SEP value
670 is consistent with the suggestion by Reames (2019) that the transition from "low-FIP" to "high-
671 FIP" elements occurs at a lower range of ionization energies for SEPs than for the solar wind.

672 **Acknowledgements:**

673 We appreciate the expertise and cooperation of the curatorial team at NASA Johnson Space
674 Center in cleaning the Genesis collector fragments. D. Ledu, F. Fortuna (CSNSM Orsay), E.
675 Briand and J.-J. Ganem (Universités Pierre et Marie Curie and Namur) are thanked for standard
676 implantations and nuclear reaction analyses. We appreciate discussions with P. Bochsler and
677 comments and suggestions by the reviewer. The UCLA ion microprobe facility is partially
678 supported by a grant from the NSF Instrumentation and Facilities program. V. S. Heber thanks
679 NASA for financial support. This work was supported by grants from the NASA Laboratory
680 Analysis of Returned Samples (LARS) program (NASA LARS 80NSSC17K0025 to D. S.
681 Burnett and A. J. G. Jurewicz). R. Wieler acknowledges the hospitality of Caltech's Division of
682 Geological and Planetary Sciences during his stay in Pasadena.

683

684

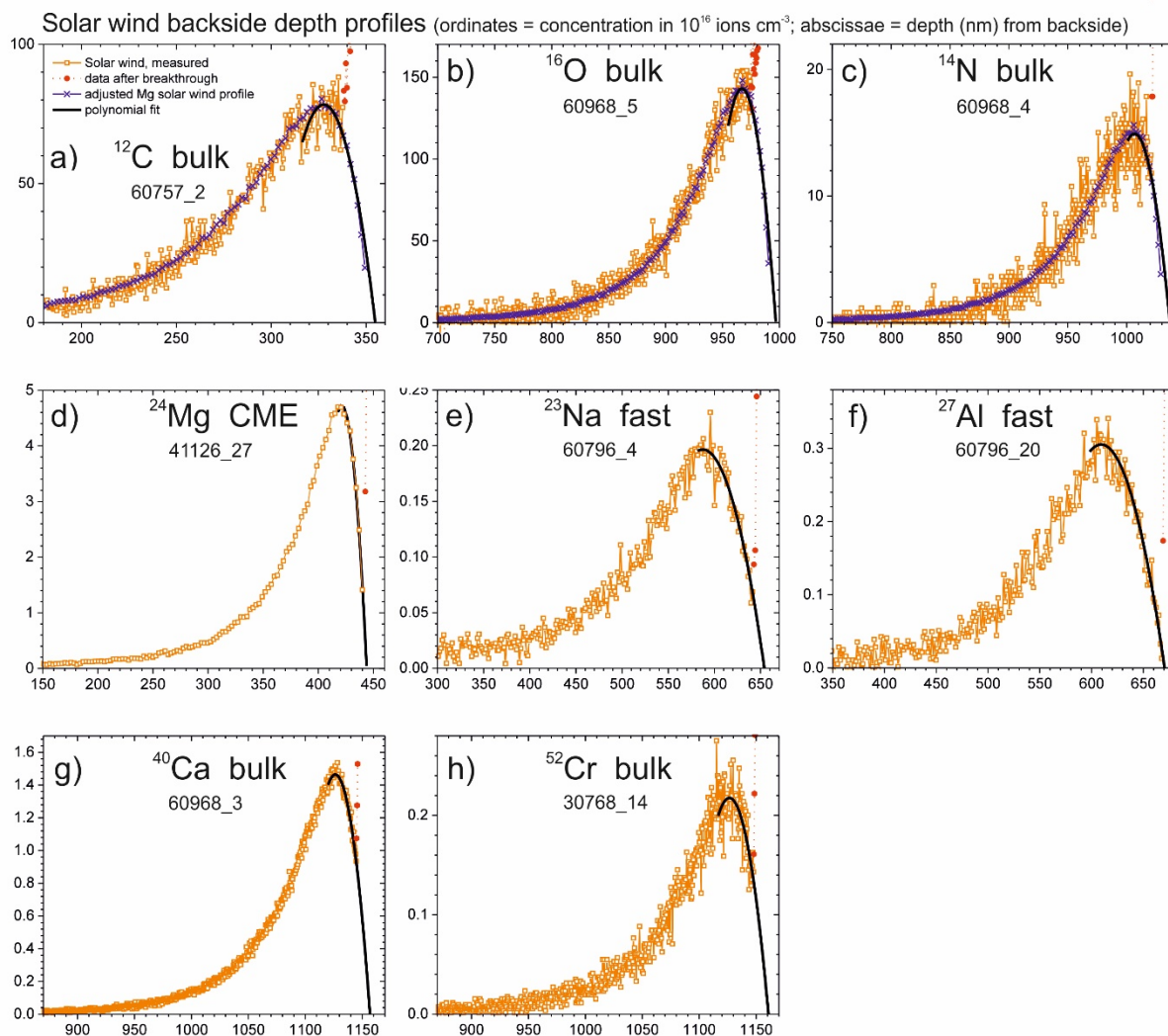
685
686
687
688
689
690
691
692
693
694
695
696
697
698
699
700
701
702
703
704
705
706
707
708
709
710
711
712
713
714
715
716
717
718
719
720
721
722
723
724
725
726

References:

- Allton, J. H., Wentworth, S. J., Rodriguez, M. C., & Calaway, M. J. 2007, in 38th Lunar and Planetary Science Conference Houston (Lunar and Planetary Institute), Abstract #2138
- Asplund, M., Grevesse, N., Sauval, A. J., & Scott, P. 2009, *Annu. Rev. Astron. Astrophys.*, 47, 481
- Basu, S., & Antia, H. M. 2008, *Physics Reports*, 457, 217
- Bodmer, R., & Bochsler, P. 2000, *J Geophys Res-Space Phys*, 105, 47
- Bochsler, P. 2009, in: *Proc. IAU Symp. 257*, 17, doi: 10.1017/s1743921309029044
- Borrini, G., Gosling, J. T., Bame, S. J., Feldman, W. C. 1982, *J. Geophys. Res.-Space Phys.*, 87, 7370
- Burnett, D. S., & Genesis Science Team, 2011, *Proc. Natl. Acad. Sci. U S A*, 108, 19147
- Burnett, D. S. 2013, *Meteorit. Planet. Sci.*, 48, 2351
- Burnett, D. S., Jurewicz, A. J. G., Woolum, D. S. et al. 2015, *Geostandards & Geoanalyt. Res.*, 39, 265
- Burnett, D. S., Guan, Y., Heber, V. S. et al., 2017, in 48th Lunar and Planetary Science Conference Houston (Lunar and Planetary Institute), abstract #1532
- Calaway, M. J., Burnett, D. S., Rodriguez, M. C. et al., 2007, in 38th Lunar and Planetary Science Conference, Houston (Lunar and Planetary Institute), abstract #1627
- Crowther, S. A., & Gilmour, J. D. 2013, *Geochim. Cosmochim. Acta*, 123, 17
- Geiss, J. 1982, *Space Sci Rev*, 33, 201
- Geiss, J., & Bochsler, P. 1985, In: *Proc Conf Isotopic Ratios in the Solar System* (Cepadues-Editions, Toulouse, France), 213
- Grimberg, A., Baur, H., Bochsler, P. et al. 2006, *Science*, 314, 1133
- Heber, V. S., Wieler, R., Baur, H. et al. 2009, *Geochim. Cosmochim. Acta*, 73, 7414
- Heber, V. S., Baur, H., Bochsler P. et al. 2012, *ApJ*, 759, 121
- Heber, V. S., Burnett, D. S., Duprat, J. et al., 2013, in 44th Lunar and Planetary Science Conference Houston (Lunar and Planetary Institute), Abstract #2540
- Heber, V. S., McKeegan, K. D., Burnett, D. S. et al. 2014a, *Chem. Geol.*, 390, 61
- Heber, V. S., McKeegan, K. D., Smith, S. et al. 2014b, in 45th Lunar and Planetary Science Conference Houston (Lunar and Planetary Institute), Abstract #1203
- Heber, V. S., McKeegan, K. D., Bochsler, P., Duprat, J., & Burnett, D. S. 2014c, in 45th Lunar and Planetary Science Conference Houston (Lunar and Planetary Institute), Abstract #2117
- Heidrich-Meisner V., Berger L., Wimmer-Schweingruber R., Wurz P., Bochsler P., Ipavich F.M., Paquette J.A., and Klecker B. 2016 AIP Conference Proceedings 1720, 040004 (2016); <https://doi.org/10.1063/1.4943815>
- Hovestadt D., Hilchenbach M., Bürgi A., Klecker B., Laeverenz P. et al.. 1995, *Solar Physics* **162**, 441-481.
- Huss, G. R., Nagashima, K., Jurewicz, A. J. G., Burnett, D. S., & Olinger, C. T. 2012, *Meteorit. Planet. Sci.*, 47, 1436
- Huss, G. R., Koeman-Shields, E., Jurewicz, A. J. G., Burnett, D. S., Nagashima, K., Oglione, R., & Olinger, C. T. 2020, *Meteorit. Planet. Sci.*, 55, 326
- Jochum, K. P., Weis, U., Stoll, B., Kuzmin, D., Yang, Q. C. et al., 2011, *Geostandards and Geoanalytical Research*, 35, 397

- 727 Jurewicz, A. J. G., Olinger, C. T., Burnett, D. S. et al. 2019, in 50th Lunar and Planetary Science
728 Conference Houston (Lunar and Planetary Institute), Abstract #2353.
- 729 Jurewicz, A. J. G., Rieck, K. D., Hervig, R. et al. 2020, *Meteorit Planet Sci*, 55, 352
- 730 Laming, J. M., Heber, V. S., Burnett, D. S. et al. 2017, *ApJL*, 851, L12
- 731 Laming, J. M., Vourlidas, A., Korendyke C. et al. 2019, *ApJ*, 879:124
- 732 Lodders, K. 2020, in: *The Oxford Research Encyclopedia of Planetary Science*, Oxford University
733 Press
- 734 Marty, B., Zimmermann, L., Burnard, P. G. et al. 2010, *Geochim. Cosmochim. Acta*, 74, 340
- 735 Marty, B., Chaussidon, M., Wiens, R. C., Jurewicz, A. J. G., & Burnett, D. S. 2011, *Science*, 332, 1533
- 736 McKeegan, K. D., Kallio, A. P. A., Heber, V. S. et al. 2011, *Science*, 332, 1528
- 737 Meshik, A., Mabry, J., Hohenberg, C. et al. 2007, *Science*, 318, 433
- 738 Meshik, A., Hohenberg, C., Pravdivtseva, O., & Burnett, D. 2014, *Geochim. Cosmochim. Acta*, 127,
739 326
- 740 Meshik, A., Pravdivtseva, O., & Burnett, D. 2020, *Geochim Cosmochim Acta*, 276, 289
- 741 Neugebauer, M. and von Steiger, R., 2001, in: *The Century of Space Science*. Kluwer Academic
742 Publishers, the Netherlands. 1115-1140.
- 743 Neugebauer, M., Steinberg, J. T. Tokar, R. L. et al. 2003, *Space. Sci. Rev.*, 105, 661
- 744 Paque J.A., Hoffman A.E., Burnett D.S., et al 2020, *Geostandards & Geoanalyt. Res.*, 44, 473, doi:
745 10.1111/ggr.12347
- 746 Pepin, R. O., Schlutter, D. J., Becker, R. H., & Reisenfeld, D. B. 2012, *Geochim. Cosmochim. Acta*, 89,
747 62
- 748 Pilleri, P., Reisenfeld, D. B., Zurbuchen, T. H. et al. 2015, *ApJ*, 812:1
- 749 Reames, D. V. 2019, *Atoms*, 7:104
- 750 Reisenfeld, D. B., Burnett, D. S., Becker, R. H. et al. 2007, *Space Sci Rev*, 130, 79
- 751 Reisenfeld, D. B., Wiens, R. C., Barraclough, B. L. et al., 2013, *Space Sci Rev*, 175, 125
- 752 Rieck, K. D. 2015, PhD thesis Arizona State University
- 753 Rieck, K. D., Jurewicz, A. J. G., Burnett, D. S. et al., 2016, in 47th Lunar and Planetary Science
754 Conference Houston (Lunar and Planetary Institute), Abstract #2922
- 755 Serenelli, A., Scott, P., Villante, F. L. et al. 2016, *Monthly Not. Royal Astron. Soc.*, 463, 2
- 756 Scott, P., Grevesse, N., Asplund, M. et al. 2015a, *A&A*, 573, A25
- 757 Scott, P., Asplund, M., Grevesse, N., Bergemann, M., & Sauval, A. J. 2015b, *A&A*, 573, A26
- 758 Steele, R. C. J., Heber, V. S., & McKeegan, K. D. 2017, *Geochim Cosmochim Acta*, 201, 245
- 759 Vogel, N., Heber, V. S., Baur, H., Burnett, D. S., & Wieler, R. 2011, *Geochim. Cosmochim. Acta*, 75,
760 3057
- 761 Vogel, N., Heber, V. S., Bochsler P. et al. 2019, *Geochim. Cosmochim. Acta*, 263, 182
- 762 von Steiger, R., Schwadron, N. A., Fisk, L. A. et al. 2000, *J. Geophys. Res.- Space Phys.*, 105, 27217
- 763 von Steiger, R., & Zurbuchen, T. H. 2016, *ApJ*, 816, 13
- 764 Wieler, R., & Baur, H. 1995, *Astrophys J*, 453, 987
- 765 Wieler, R., Kehm, K., Meshik, A. P., & Hohenberg, C. M. 1996, *Nature*, 384, 46

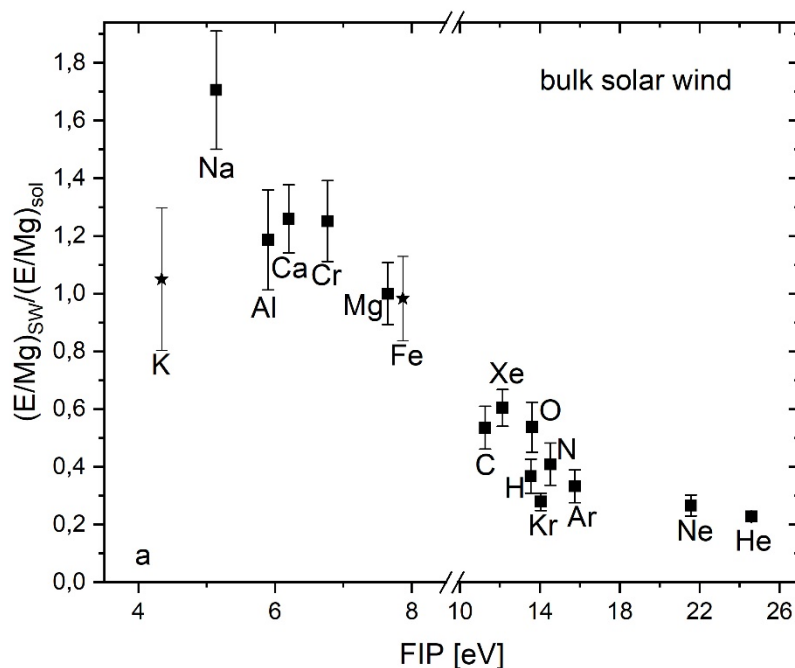
- 766 Ziegler, J. F., Ziegler, M. D., & Biersack, J. P. 2010, Nuclear Instruments & Methods in Physics
767 Research Section B-Beam Interactions with Materials and Atoms, 268, 1818
- 768 Zinner, E. 1983, J. Electrochem. Soc., 130, C199

769 **Figure 1:**

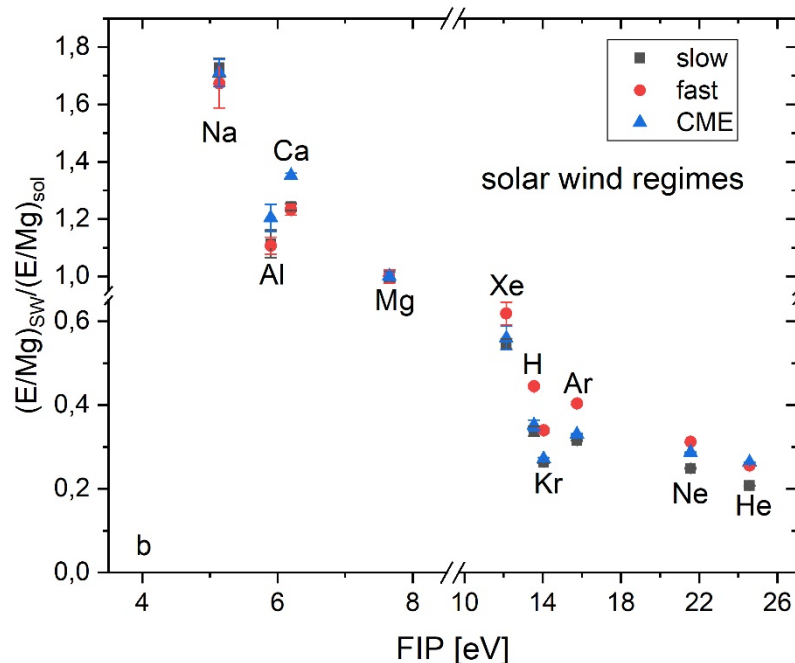
770

771 **Figure 1:** Examples of measured and extrapolated solar wind profiles of different elements in Bulk SW
 772 targets or different SW regimes (sample details given in Tables 4 and 5 in the Appendix). Ordinates
 773 represent concentrations in 10^{16} ions cm^{-3} , abscissae the depth in nm measured from the backside
 774 of the collector. Measured Solar wind data are shown as orange squares, red dots represent data at and
 775 after breakthrough, i.e. when the primary ion beam first penetrates the collector surface. The polynomial
 776 fit of the extrapolation of the profiles prior to breakthrough is shown as black solid line.

777

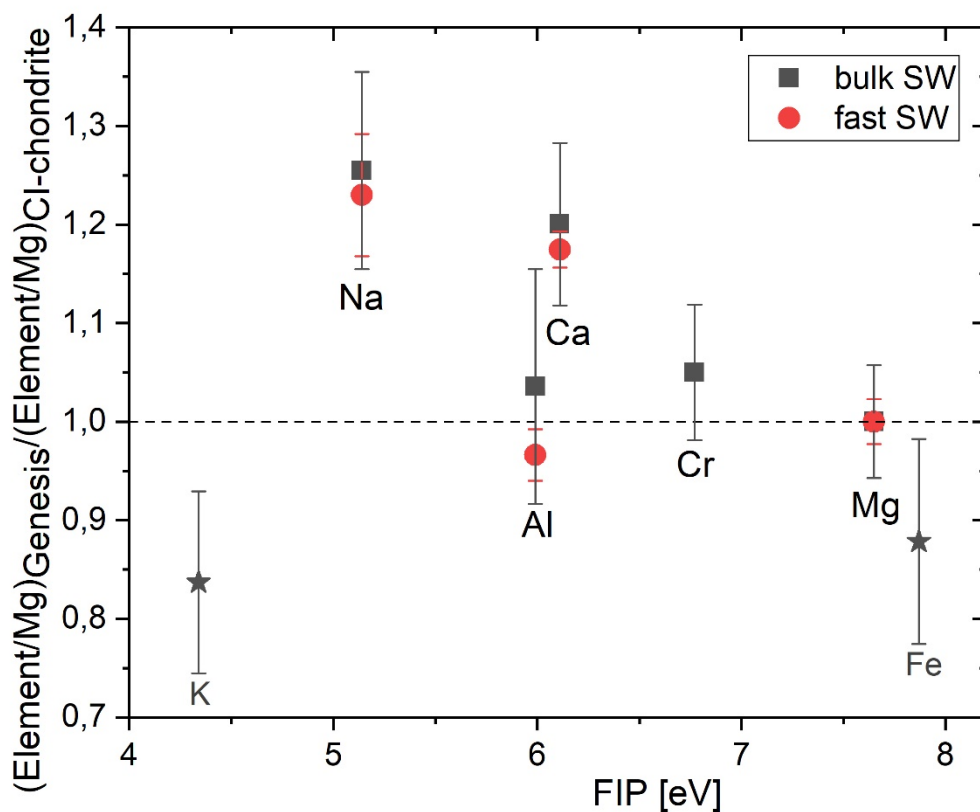
778 **Figure 2:**

779



780

781 **Figure 2:** 2a (upper panel): Fluence ratios (elements/Mg) in Genesis Bulk-SW targets normalized to
 782 solar ratios (Table 7, Appendix). Values from this work and H are from Table 1. Data for K (Rieck
 783 2015) and Fe (Burnett et al. 2017) in Bulk SW targets (a, upper panel) are shown by asterisks. Error
 784 bars for Bulk targets reflect the total uncertainties given in Table 1 and 1σ uncertainties of solar ratios.
 785 2b (lower panel): Fluence ratios (elements/Mg) in Genesis regime targets. Here, only the analytical
 786 uncertainties (\pm in Table 1), with uncertainties for Mg not propagated, are shown. FIPs of some elements
 787 in Fig. 2b slightly shifted to increase visibility. Ordinate data are shown in Table 8 (Appendix). The FIP
 788 plots for the different regimes are strikingly similar, particularly for low FIP elements. Fast solar wind
 789 has been regarded as least fractionated. Our results confirm this, but the decrease in fractionation is
 790 relatively small.

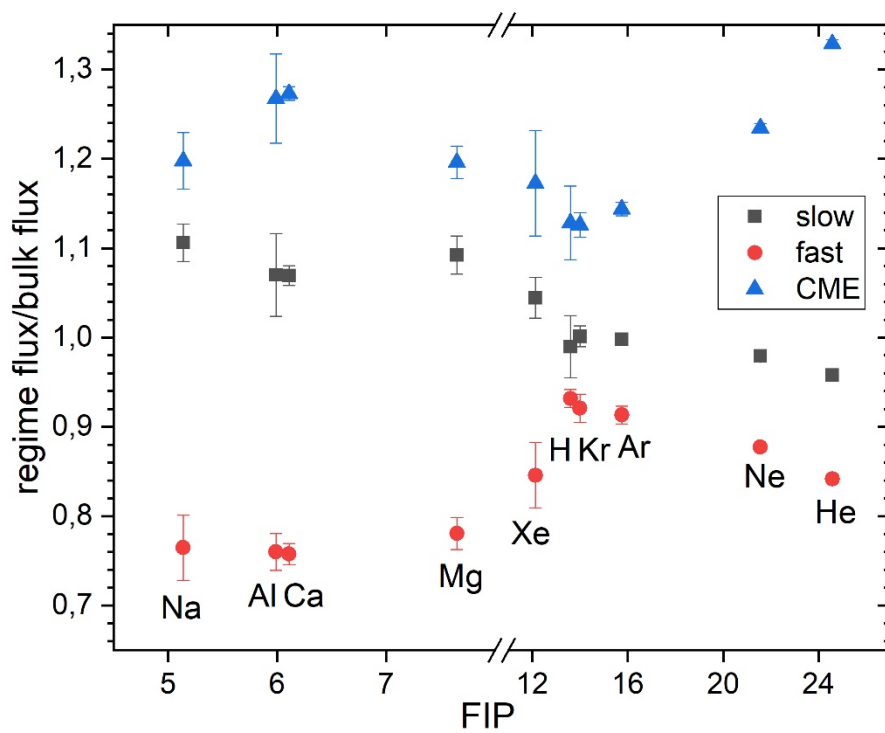
791 **Figure 3:**

792

793

794 **Figure 3:** Fluence ratios (elements/Mg) in Genesis Bulk-SW and Fast-SW targets normalized to
 795 respective ratios in CI chondrites (Lodders 2020). Error bars for Bulk targets reflect the total
 796 uncertainties given in Table 1 and 1σ errors for CI chondrites. Error bars for Fast SW reflect only
 797 analytical uncertainties (\pm in Table 1). For clarity, besides Bulk SW data only those for the Fast SW
 798 regime, thought to be least fractionated, are shown, but the good agreement with CI abundances also
 799 holds for the other two regimes.

800

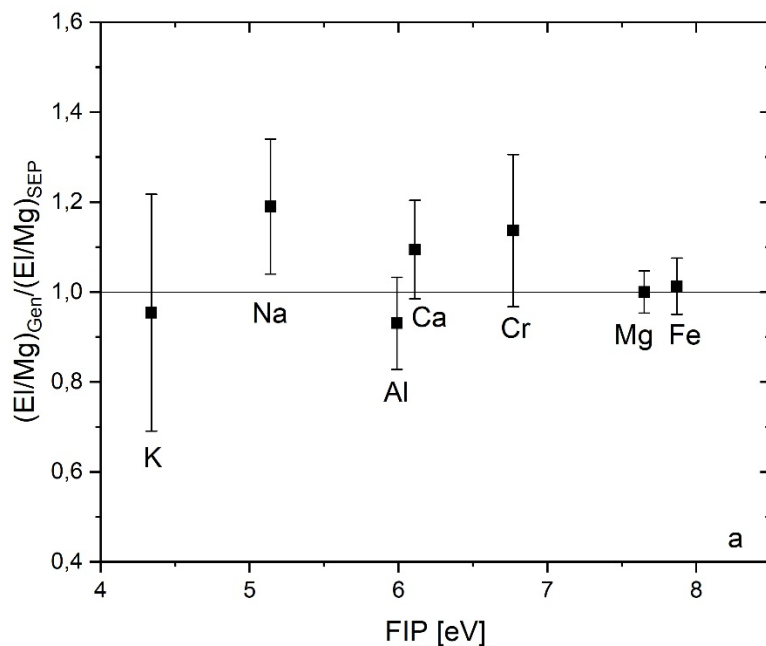
801 **Figure 4:**

802

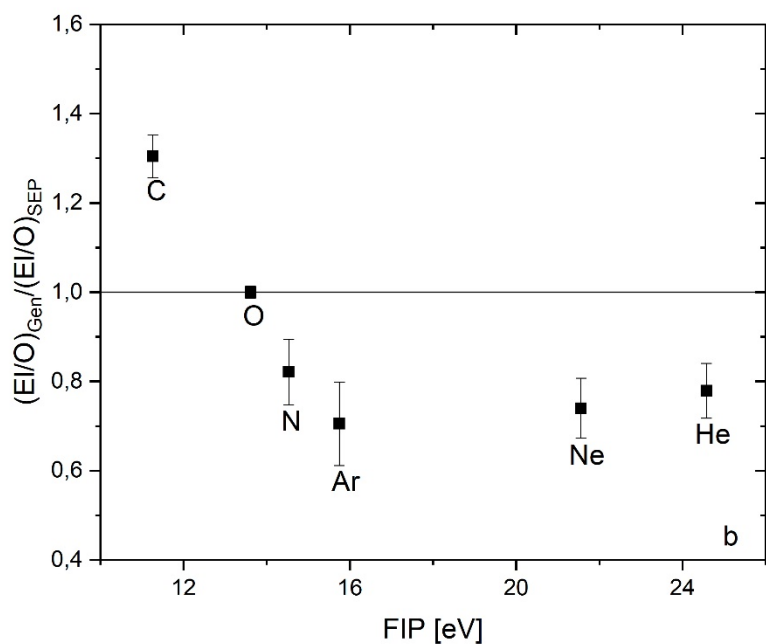
803 **Figure 4:** Ratios of elemental fluxes in Genesis regimes over those in Genesis Bulk solar wind (Bulk
 804 SW data obtained from weighted regime target data). Data from Table 1.

805

806

807 **Figure 5:**

808



809

810 **Figure 5:** Ratios of elemental abundances in Genesis Bulk SW targets and Solar Energetic Particles
 811 (SEP). For low-FIP elements (panel a) Mg is used for normalization, high-FIP elements (panel b) are
 812 normalized to O. SEP data are from Reames (2019). Total errors (Table 1) used for Genesis data.

813

Table 1
Solar wind element fluences measured in Genesis collectors

Element	FIP (eV)	Solar wind fluence (ions cm ⁻²)									Reference	
		Bulk	±	Total error	Slow	±	Fast	±	CME	±		
C	11.26	6.41E1	0.32E1	0.37E1								
N	14.53	1.23E1	0.03E1	0.13E1								
O	13.61	1.17E1	0.12E1	0.12E1								
Na	5.14	1.23E1	0.04E1	0.08E1	5.18E1	0.10E1	3.36E1	0.17E1	3.25E1	0.09E1		
Mg	7.65	1.73E1	0.04E1	0.06E1	7.19E1	0.14E1	4.82E1	0.11E1	4.56E1	0.07E1		
Al	5.99	1.42E1	0.05E1	0.15E1	5.54E1	0.24E1	3.69E1	0.10E1	3.80E1	0.15E1		
Ca	6.11	1.17E1	0.04E1	0.06E1	4.80E1	0.05E1	3.19E1	0.05E1	3.31E1	0.02E1		
Cr	6.77	2.32E1	0.05E1	0.11E1								
H	13.6	1.634E	0.014E	0.164E	0.624E	0.022E	0.551E	0.006E	0.412E	0.015E	1	
He	24.58	8.293E	0.022E	0.15E1	3.152E	0.012E	2.597E	0.006E	2.532E	0.008E	2	
Ne	21.56	1.359E	0.006E	0.032E	5.292E	0.028E	4.447E	0.020E	3.864E	0.016E	2	
Ar	15.75	3.547E	0.017E	0.070E	1.398E	0.007E	1.200E	0.013E	0.928E	0.006E	2	
Kr	13.99	2.20E7	0.12E7	0.16E7	8.66E6	0.10E6	7.47E6	0.13E6	5.64E6	0.07E6	3	
Xe	12.13	4.87E6	0.29E6	0.38E6	1.83E6	0.04E6	1.39E6	0.06E6	1.19E6	0.06E6	3	

Notes. Isotopic compositions used to calculate element fluences from measured data are from Heber et al. (2009) for He, Ne, Ar, Meshik et al. (2014, 2020) for Kr, Xe, McKeegan et al. (2011) for O; Marty et al. (2011) for N. Terrestrial values adopted for C, Mg, Ca, Cr. Noble gas fluences were recalculated from original references (see Appendix, A4). Stated uncertainties are 1 σ (including those of H from ref. #1, total error for H in Bulk SW includes 10% uncertainty of H₂O concentration in apatite standard).

Errors in columns "±" do not include the systematic uncertainties of the standards, since these cancel when comparing differences in fluences and element ratios among different regimes. The total error including errors in standard calibration is shown for the Bulk fluences.

Exposure durations: Bulk SW = 852.83 d, Fast SW = 313.01 d, Slow SW = 333.67 d; CME = 193.25 d (Reisenfeld et al. 2013)

References. (1) Huss et al. 2020 (2) Heber et al. 2009 (3) Vogel et al. (2019).

Table 2

Comparison of low-FIP element ratios in Genesis regimes

Regime	Na/Mg	Al/Mg	Ca/Mg
Slow	0.0716	0.0771	0.0668
Fast	0.0697	0.0766	0.0662
CME	0.0597	0.0833	0.0726
average regimes	0.0664	0.0790	0.0685
stdev (%)	11.2%	4.8%	5.2%
Bulk	0.0711	0.0821	0.0676

Notes: Errors in individual element/Mg values are 1.6-4.6%.

Table 3
Comparison of elemental abundance ratios in ACE & Genesis

Bulk SW	ACE ^a	\pm^b	Genesis	\pm
Fe/Mg	0.98	0.20	0.746	0.039
C/Mg	4.39	0.88	3.71	0.25
O/Mg	6.64	1.00	6.76	0.74
Ne/Mg	0.749	0.15	0.786	0.033
He/Mg	600	120	479	20

Regimes/Bulk SW	Slow SW/Bulk SW		FastSW/Bulk SW		CME/Bulk SW	
	ACE ^a	Genesis	ACE ^a	Genesis	ACE ^a	Genesis
Ne/Mg	0.91	0.94	1.06	1.17	1.06	1.08
He/Mg	1	0.91	1.07	1.12	0.89	1.16

Notes. a) ACE data from ref. (1) measured by the SWICS instrument during time intervals corresponding to the respective collection periods of the Genesis Bulk or regime targets. Errors for Genesis data are total errors from Table 1.

b) Instrumental uncertainties as reported by ref. (1).

Reference: (1) Pilleri et al. (2015)

Electronic Appendix to:

**Elemental abundances of major elements in the solar wind as measured in
Genesis targets and implications on solar wind fractionation**

Veronika S. Heber, Kevin D. McKeegan, Robert C. J. Steele, Amy J. G. Jurewicz,
Karen Rieck, Yunbin Guan, Rainer Wieler, Donald S. Burnett

Submitted to *Astrophysical Journal*, Sept. 8, 2020, revised version submitted Oct. 27, 2020

References in the Appendix are included in references for manuscript text.

A1. Basic analytical procedures

Artificial ion implants into Si served as reference. One minor isotope of the element of interest (except for Cr and the monoisotopic elements Al and Na) with approximately-known nominal fluences was implanted. Profiles of the reference implants, conventionally sputtered from the front-side, were routinely measured prior to and after each solar wind profile for the positive ions (Na, Mg, Al, Ca, and Cr) in a standard-sample bracketing mode, or several times per day for the negative ions (C, N, and O). The depth of raster pits in the reference implants was measured by a MicroXam Surface Mapping Microscope and/or a Zygo optical surface profiler (Heber et al 2014a).

All analyses of reference and solar wind profiles were done under identical conditions in each given session. The standard-sample bracketing technique allowed us to reduce uncertainties of calibration factors due to instrumental variations, especially important for the regime samples which were expected to show abundance differences of a few percent at best if low-FIP elements are unfractionated relative to each other.

A2. Data reduction

Measured signals of the isotope of interest were corrected for the effective dead time of the counting system and for background contributions. No correction was made for instrumental mass fractionation between the isotopes measured in the reference implant and the sample, respectively, as such effects are small compared to the overall uncertainty of the solar wind fluence determinations.

From the reference implants sputter rates (S) and Solar Wind fluences (F_i) were obtained according to equations (1) & (2):

$$S = x/t \quad (1)$$

with x being the measured pit depth and t the total sputter time of a profile. Sputter rates obtained for the reference implants were used for the sample backside profiles measured prior to and afterwards. A sensitivity factor, RSF, is used to relate implant standard secondary ion intensity, normalized to the matrix element Si, to standard implant fluence (Burnett et al. 2015; Heber et al. 2014a).

The unknown solar wind fluence (F_i) of an isotope of interest is calculated from its depth profile according to equation 2:

$$F_i = \text{RSF} \times \int (n_i / n_{\text{Si}}) dx. \quad (2)$$

with n_i and n_{Si} being the ion intensities in counts per second of the isotope of interest and the matrix element Si, respectively. Equation (2) is also used with a known implant standard fluence to determine RSF.

For species implanted to depths as shallow as SW ions, measured backside depth profiles never reach the solar wind surface. Even low energy primary ions of 5 – 7 keV as used here penetrate by about 5 to 10 nm into the target. This penetration causes epoxy and other contaminants from the original surface to be backward-gardened and eventually dominate the secondary ion signal. At this point a measurement had to be stopped, and an extrapolation of the profile to the solar wind surface is required to determine an extrapolated surface correction (F_E) to the measured profile.

Fig. 1 in the main text shows, for each element, one measured backside profile; further examples (listed in Table 5) are given by Heber et al. (2014a). The most complete profiles were obtained for the positive ions, with the extrapolated fluence (F_E) in the unrecovered near-surface portion on average contributing only ~5% to the total fluence (F_T). The most complete measured profiles were obtained for Mg ($F_E \leq 1.1\%$ of F_T). The distance between the last measured “good” data point to the extrapolated original surface (D_E) was on average 10 nm. The negative ion profiles (C, N, O) are characterized by earlier breakthroughs, at around the depth of the

maximum SW concentration. This is the result of the high abundances of these elements on surfaces (e.g., the uppermost 2 nm of metallic Si consist of a native SiO₂ layer) and because these elements are main constituents of epoxies.

The near-surface portions of the depth profiles were extrapolated as follows (cf. Heber et al. 2014a for more details): The nearly complete Mg profiles indicate that the measured data between the peak region and the original collector surface are well described by a quadratic polynomial. Such polynomials were therefore fitted to all profiles whose measured data extended from the peak to at least one third of the distance towards the collector surface. This included 30 of the 39 profiles obtained with positive ions (Na, Mg, Al, Ca, and Cr). For all Na profiles the distance to the collector surface was set equal to that of the concomitantly measured Mg profile, as Na always broke-through earlier than Mg by a few nm. Data coverage on the collector surface side of the profile peaks was insufficient for this approach for nine profiles obtained with positive ions and all negative ion profiles. In these cases we adopted the shape of a more complete profile of the same element (or sometimes of Mg) obtained in another analysis or of Mg from the same solar wind regime (main text, Figs. 1a-c). This approach is justified as our data and simulations by the SRIM code (Stopping and Range of Ions in Matter; Ziegler et al. 2010) show that depth distributions and peak depths of different elements implanted with the same energy distribution are similar to each other. F_E (given as the % of F_T) and D_E values as well as the applied extrapolation method are given in Table 5.

Total fluences (F_T) were obtained by adding the extrapolated fluence F_E integrated over the fit polynomial between break-through and collector surface to the measured fluence (integrated over the measured data). Finally, small corrections to the fluences were made for backscatter loss upon SW implantation into the Si target. The backscatter correction factors were obtained by SRIM using the solar wind speed distributions at the time of the Genesis collection period (Reisenfeld et al. 2013).

Table 4 shows the details of each backside SIMS analysis and each individual fluence.

Table 5 gives additional details.

Table 4						
Fluences measured in each individual backside SIMS analysis						
Analysis# & session date	Isotope	regime	Fluence ^a (ions cm ⁻²)	Error, 1 σ (ions cm ⁻²)	error includes	
1 (10/2010)	¹⁶ O	bulk	1.04E13	1.39E11	RSF, S	
2 (10/2010)	¹⁶ O	bulk	1.14E13	1.53E11	RSF, S	
average 1&2			1.09E13	7.12E11	stdev. of 2 analyses	
3 (06/2012)	¹⁶ O	bulk	1.20E13	2.00E11	RSF, S	
4 (06/2012)	¹⁶ O	bulk	1.22E13	2.03E11	RSF,S	
5 (06/2012)	¹⁶ O	bulk	1.34E13	2.23E11	RSF, S	
average 3-5			1.26E13	7.5E11	stdev. of 3 analyses	
average ¹⁶O bulk			1.17E13	1.25E12	stdev. 2 session av., RSF, S + 2.5% ref. calibration ^b	
7 (10/2010)	¹² C	bulk	6.86E12	1.21E10	RSF, S	
8 (10/2010)	¹² C	bulk	6.14E12	1.08E10	RSF, S	
9 (10/2010)	¹² C	bulk	6.17E12	1.28E10	RSF, S	
10 (10/2010)	¹² C	bulk	6.46E12	1.34E10	RSF, S	
11 (10/2010)	¹² C	bulk	6.37E12	1.33E10	RSF, S	
12 (10/2010)	¹² C	bulk	5.23E12	6.68E10	RSF, S	
13(10/2010)	¹² C	bulk	5.57E12	1.16E10	RSF, S	
average 7-13			6.12E12	5.50E11	stdev. of 7 analyses	
14 (06/2012)	¹² C	bulk	6.69E12	9.24E10	RSF, S	
15 (06/2012)	¹² C	bulk	6.42E12	6.57E9	RSF, S	
average 14,15			6.56E12	1.91E11	stdev. of 2 analyses	
average ¹²C bulk			6.34E12	3.61E11	stdev. 2 session av., RSF, S + 2.8% ref. calibration ^b	

16 (10/2010)	¹⁴ N	bulk	1.25E12	3.31E10	RSF, S
17 (10/2010)	¹⁴ N	bulk	1.55E12	4.11E10	discarded ^c
18 (10/2010)	¹⁴ N	bulk	1.24E12	3.27E10	RSF, S
average 16,18			1.24E12	9.23E9	stdev. of #16&18
19 (06/2012)	¹⁴ N	bulk	1.23E12	1.06E10	RSF, S
20 (06/2012)	¹⁴ N	bulk	1.21E12	1.09E10	RSF, S
21 (06/2012)	¹⁴ N	bulk	1.21E12	1.16E10	RSF, S
22 (06/2012)	¹⁴ N	bulk	1.21E12	1.10E10	RSF, S
average 19-22			1.22E12	1.18E10	stdev. of 4 analyses
average ¹⁴N bulk			1.23E12	1.26E11	stdev. 2 session av., RSF, S + 10% (missing ref. calib.)
23 (02/2013)	²⁷ Al	bulk	1.40E11	3.94E9	RSF, S
24 (02/2013)	²⁷ Al	bulk	1.41E11	9.90E9	RSF, S
25 (04/2013)	²⁷ Al	bulk	1.43E11	3.66E9	RSF, S
26 (04/2013)	²⁷ Al	bulk	1.46E11	3.18E9	RSF, S
average ²⁷Al bulk^d			1.42E11	1.52E10	stdev. 4 analyses, RSF, S + 10% (missing ref. calib.)
27 (02/2013)	²⁷ Al	fast	3.71E10	1.09E9	RSF, S
28 (02/2013)	²⁷ Al	fast	3.70E10	1.09E9	RSF, S
29 (04/2013)	²⁷ Al	fast	3.65E10	7.70E8	RSF, S
average ²⁷Al fast^d			3.69E10	9.83E8	stdev. of 3 analyses, RSF, S
30 (02/2013)	²⁷ Al	CME	3.62E10	1.02E9	RSF, S
31 (02/2013)	²⁷ Al	CME	3.85E10	1.08E9	RSF, S
32 (04/2013)	²⁷ Al	CME	3.81E10	6.93E8	RSF, S
average ²⁷Al CME^d			3.80E10	1.49E9	stdev. of 3 analyses, RSF, S
33 (02/2013)	²⁷ Al	slow	5.47E10	1.54E9	RSF, S
34 (02/2013)	²⁷ Al	slow	5.48E10	2.00E9	RSF, S
35 (04/2013)	²⁷ Al	slow	5.83E10	8.60E8	RSF, S
average ²⁷Al slow^d			5.54E10	2.43E9	stdev. of 3 analyses, RSF, S
36 (02/2013)	²⁴ Mg	bulk	1.39E12	1.91E10	RSF, S
37 (02/2013)	²⁴ Mg	bulk	1.35E12	1.44E10	RSF, S

average ^{24}Mg bulk^d			1.37E12	4.89E10	stdev. of 2 analyses, RSF, S + 2.8% ref. calibration ^e
38 (02/2013)	^{24}Mg	fast	3.76E11	5.10E9	RSF, S
39 (02/2013)	^{24}Mg	fast	3.86E11	5.01E9	RSF, S
average ^{24}Mg fast^d			3.81E11	8.65E9	stdev. of 2 analyses, RSF, S
40 (02/2013)	^{24}Mg	CME	3.64E11	3.75E9	RSF, S
41 (02/2013)	^{24}Mg	CME	3.57E11	3.81E9	RSF, S
42 (02/2013)	^{24}Mg	CME	3.56E11	3.80E9	RSF, S
average ^{24}Mg CME^d			3.60E11	5.71E9	stdev. of 3 analyses, RSF, S
43 (02/2013)	^{24}Mg	slow	5.75E11	7.92E9	RSF, S
44 (02/2013)	^{24}Mg	slow	5.63E11	5.35E9	RSF, S
average ^{24}Mg slow^d			5.68E11	1.08E10	stdev. of 2 analyses, RSF, S
45 (02/2013)	^{23}Na	bulk	9.76E10	1.57E9	RSF, S
46 (02/2013)	^{23}Na	bulk	1.02E11	1.98E9	RSF, S
average ^{23}Na bulk^d			1.00E11	1.07E10	stdev. 2 analyses, RSF, S + 10% (missing ref. calib.)
47 (02/2013)	^{23}Na	fast	2.82E10	5.96E8	RSF, S
48 (02/2013)	^{23}Na	fast	2.65E10	5.50E8	RSF, S
average ^{23}Na fast^d			2.73E10	1.34E9	stdev. of 2 analyses, RSF, S
49 (02/2013)	^{23}Na	CME	2.70E10	5.19E8	RSF, S
50 (02/2013)	^{23}Na	CME	2.63E10	5.10E8	RSF, S
51 (02/2013)	^{23}Na	CME	2.60E10	5.04E8	RSF, S
average ^{23}Na CME^d			2.64E10	7.40E8	stdev. of 3 analyses, RSF, S
52 (02/2013)	^{23}Na	slow	4.21E10	7.90E8	RSF, S
53 (02/2013)	^{23}Na	slow	4.25E10	6.82E8	RSF, S
average ^{23}Na slow^d			4.21E10	7.88E8	stdev. of 2 analyses, RSF, S
54 (04/2013)	^{40}Ca	bulk	1.11E11	1.88E9	RSF, S
55 (04/2013)	^{40}Ca	bulk	1.16E11	7.38E8	RSF, S
average ^{40}Ca bulk^d			1.13E11	5.99E9	stdev. of 2 analyses, RSF, S + 4.1% ref. calibration ^e

56 (04/2013)	⁴⁰ Ca	fast	3.09E10	5.11E8	RSF, S
57 (04/2013)	⁴⁰ Ca	CME	3.21E10	2.03E8	RSF, S
58 (04/2013)	⁴⁰ Ca	slow	4.62E10	3.46E8	RSF, S
59 (04/2013)	⁴⁰ Ca	slow	4.67E10	4.48E8	RSF, S
average ⁴⁰Ca slow^d			4.65E10	5.29E8	stdev. of 2 analyses, RSF, S
60 (04/2013)	⁵² Cr	bulk	1.95E10	3.06E8	RSF, S
61 (04/2013)	⁵² Cr	bulk	1.95E10	5.62E8	RSF, S
average ⁵²Cr bulk⁵			1.95E10	9.40E8	stdev. of 2 analyses, RSF, S + 4.3% ref. calibration ^e

Analysis number in column 1 used to identify analysis in Table 6

^a Fluences (for isotopes measured, not total elements) backscatter-corrected according to prevailing solar wind conditions during collection. Uncertainties include the standard deviations of RSF and S (see section A2) measured in reference implants for the elements measured as positive ions. For C, N, and O we include the standard deviation of RSF and S over a day

^b Uncertainty of reference calibration calculated from Orsay implant data (Heber et al. 2014a)

^c Measurement interrupted near concentration peak. Onset of break-through difficult to assess

^d Average fluences for positive ion profiles weighted based on completeness of data coverage

^e Uncertainties of reference calibrations include standard deviations of n analyses of standard glasses (Table 4), concentration uncertainties of standard elements in the glasses and uncertainties of pit depths measured with a profilometer

Table 5
Details of individual backside SIMS analyses

Analysis #	NASA sample code	D _E (nm)	F _E (%)	method to account for missing data	reference implant
1&2 (¹⁶ O)	30767	30/24	21/17	Mg analysis #39, 2nd order polynomial	Orsay implant K09-07_18O ¹⁵ N during measurement with fluence adjusted
3-5 (¹⁶ O)	30767	22/24/22	15/17/15	Mg analysis #39, 2nd order polynomial	Orsay K09-07_18O ¹⁵ N during measurement with fluence adjusted
7-11 (¹² C)	60757	25/17/23 /25/22	18/11/16/18/ 15	Mg analysis #39, 2nd order polynomial	Orsay implant (K09-05_05_13C during measurement with fluence adjusted
12-13 (¹² C)	30767	26/31	20/24	Mg analysis #39, 2nd order polynomial	Orsay implant (K09-05_05_13C during measurement with fluence adjusted
14-15 (¹² C)	60968	23/22	17/15	Mg analysis #39, 2nd order polynomial	Orsay implant (K09-05_05_13C during measurement with fluence adjusted
16-18 (¹⁴ N)	60757	13/21/15	6/15/8	K 04_2013_AlCa	EAG 4257 (K09-07_18O ¹⁵ N during measurement with fluence adjusted
19-22 (¹⁴ N)	60968	14/12/14 /16	7/5/7/8	Mg analysis #39, 2nd order polynomial	EAG 4257 (K09-07_18O ¹⁵ N during measurement with fluence adjusted
23 (²⁷ Al) bulk	60514	12	5	2nd order polynomial	K 04_2013_AICa08_Al used during measurement with fluence adjusted
24 (²⁷ Al) bulk	60514	11	7	Asym2sig (Origin®), 2nd order polynomial	K 04_2013_AICa08_Al used during measurement with fluence adjusted
25 (²⁷ Al) bulk	30768	15	8	Asym2sig (Origin®), 2nd order polynomial	K 04_2013_AICa08_Al used during measurement with fluence adjusted
26 (²⁷ Al) bulk				Mg analysis #39, 2nd order polynomial	K 04_2013_AICa08_Al used during measurement with fluence adjusted
27-29 (²⁷ Al) fast	60796	7.3/2.8/ 6.5	0.6/0.1/0.5	2nd order polynomial	K 04_2013_AICa08_Al used during measurement with fluence adjusted

30 (²⁷ Al) CME	41126	18	10	Al analysis #31, 2nd order polynomial	K 04_2013_AIC 08_Al used during measurement with fluence adjusted
31 (²⁷ Al) CME	41126	3.4	0.6	2nd order polynomial	K 04_2013_AIC 08_Al used during measurement with fluence adjusted
32 (²⁷ Al) CME	41133	3.9	0.7	2nd order polynomial	K 04_2013_AIC
33-34 (²⁷ Al) slow	60833	1.4/4.5	0.2/2	2nd order polynomial	K 04_2013_AIC 08_Al used during measurement with fluence adjusted
35 (²⁷ Al) slow	60449	8.7	6	Al analysis #33, 2nd order polynomial	K 04_2013_AIC
36-37 (²⁴ Mg) bulk	60514	4.8/3.2	1.1/0.5	2nd order polynomial	K 02_2010 ²⁵ Mg 02_2013 Na ²⁵ Mg during measurement fluence adjusted
38-39 (²⁴ Mg) fast	60796	1.6/4.5	0.0/0.3	2nd order polynomial	K 02_2010 ²⁵ Mg 02_2013 Na ²⁵ Mg during measurement fluence adjusted
40-41 (²⁴ Mg) CME	41126	5.2/3.9	1.2/0.9	2nd order polynomial	K 02_2010 ²⁵ Mg 02_2013 Na ²⁵ Mg during measurement fluence adjusted
42 (²⁴ Mg) CME	41126			Mg (41126, analysis 41), 2nd order polynomial	K 02_2010 ²⁵ Mg 02_2013 Na ²⁵ Mg during measurement fluence adjusted
43-44 (²⁴ Mg) slow	60833	11.1/2.4	6.9/0.5	2nd order polynomial	K 02_2010 ²⁵ Mg 02_2013 Na ²⁵ Mg during measurement fluence adjusted
45-46 (²³ Na) bulk	60514	12.8/11.0	6/9	2nd order polynomial, end of profile set by Mg of same measurement	K 02_2013 Na ²³ Mg
47-48 (²³ Na) fast	60796	12.9/9.6	2/1.1	2nd order polynomial, end of profile set by Mg of same measurement	K 02_2013 Na ²³ Mg
49-50 (²³ Na) CME	41126	22.9/9.8	16/4	2nd order polynomial, end of profile set by Mg of same measurement	K 02_2013 Na ²³ Mg
51 (²³ Na) slow	41126	31.7	14	Mg of same measurement, 2 nd order polynomial	K 02_2013 Na ²³ Mg

52-53 (²³ Na) slow	60833	9.6/28.5	5/33	2nd order polynomial, end of profile set by Mg of same measurement	K 02_2013 Na ²³
54-55 (⁴⁰ Ca) bulk	60998	3.3/12.2	0.7/5	2nd order polynomial	K 04_2013_AIC
56 (⁴⁰ Ca) fast	60796	7.0	0.9	2nd order polynomial	K 04_2013_AIC
57 (⁴⁰ Ca) CME	41133	4.3	0.9	2nd order polynomial	K 04_2013_AIC
58-59 (⁴⁰ Ca) slow	60449	15.1/10.1	16/9	Asym2sig (Origin® fit) of Mg analysis #44, 2nd order polynomial	K 04_2013_AIC
60-61 (⁵² Cr) bulk				2nd order polynomial	CEI 62Ni, 52Cr and L52 (with fl adjusted

Notes. Analysis # in column 1 refers to column 1 in Table 5

^a D_E = Extrapolated distance to target surface of last measured point before break-through

^b F_E = Extrapolated fluence of unrecovered near surface portion as fraction of total fluence F_T

Reference. (1) Heber et al. (2014a)

A3. Absolute calibration of the reference implant fluences

Solar wind fluences were calibrated against reference implants with nominal fluences on the order of 10^{13} ions cm^{-2} for positive ions and $(0.5 - 1) \times 10^{15}$ ions cm^{-2} for negative ions. These nominal fluences have uncertainties of $\sim 10\%$, sometimes more, and require independent calibration. Heber et al. (2014a) absolutely calibrated some reference implants. Briefly, the C and O reference implant fluences were cross-calibrated with independent implantations at the Centre de Sciences Nucléaires et de Sciences de la Matière (CSNSM) Orsay (France) and the accuracy of the ^{18}O fluence was further cross-checked by nuclear reaction analysis at the Université de Namur (Belgium). For N we relied on one ^{15}N implant that contained also implanted ^{18}O and ^{13}C with fluences in agreement with those determined in Orsay to within 4% and 2%, respectively, and added an uncertainty of 10% to account for the missing absolute calibration. The Mg, Cr, and Ca reference implants were calibrated using standard glasses with known concentration of these elements. Glasses and Si wafers that were used as reference during the solar wind analysis were simultaneously implanted (Burnett et al. 2015). Absolutely calibrated fluences of C and O in the Orsay implants and the resulting differences to our reference implants are given in Table 4 in Heber et al. (2014a), while Table 6 gives the updated results for Mg, Ca, and Cr.

The Na implant calibration is from Rieck (2015) (see also Rieck et al. 2016). An absolute calibration was obtained by Rutherford Backscattering Analysis on a nominal $1\text{e}16/\text{cm}^2$ Na implant into diamond-like-C (DLC) giving a calibrated fluence of $1.136 \pm 0.010 \times 10^{16}/\text{cm}^2$ (error is 1 sigma mean of 10 spectra). Si samples co-implanted with the DLC have the same fluence (Burnett et al., 2015). The K Al 42Ca 2013 nominal $1\text{E}13$ implant used as a standard for solar wind Na analyses cannot be intercalibrated directly with the $1\text{E}16$ implant; our SIMS dynamic range is insufficient because of our inability to do accurate deadtime corrections with a rastered beam. Consequently, an intermediate ("Stevie") nominal $1\text{E}14$ implant was calibrated

relative to the 1E16 implant. Separately, the 2013 Na implant was calibrated relative to Stevie. The fluence of the 2013 Na implant is $1.230 \pm 0.66 \times 10^{13}/\text{cm}^2$. This is slightly revised from the 1.28 value given in Rieck (2015).

Using the approach of Burnett et al. (2015), a nominal $1 \times 10^{13}/\text{cm}^2$ ^{42}Ca implant Si standard was coimplanted with a sample of NIST 93a standard glass as the absolute reference material. The Ca concentration of the 93a glass sample was measured by electron microprobe (emp) at Caltech to be 86.8 ± 1.4 ppm; relative to this, SIMS analyses of the ^{42}Ca -implanted 93a glass sample yielded a ^{42}Ca implant fluence of $1.18 \times 10^{13}/\text{cm}^2$. Allowing for the error in the emp analysis, the ^{42}Ca implant fluence is $1.18 \pm 0.05 \times 10^{13}/\text{cm}^2$. At this relatively low Ca concentration, the emp Ca analyses were not routine; variable emp Ca concentrations were measured adjacent to SIMS pits which showed a uniform $^{40}\text{Ca}/^{28}\text{Si}$ counting rate ratio; however, 86.8 ppm within error defined a baseline value for around 2/3 of the analyses and the rest were higher. Detailed emp analyses ruled out significant effects from Na or B migration; the high values very likely reflect Ca surface contamination. Simultaneous SIMS/emp analyses show similar contamination effects for Al in olivine at ≈ 100 ppm levels (Paque et al. 2020). The calibrated ^{42}Ca implant Si sample coimplanted with 93a was used as a standard for solar wind analyses.

Table 6. Calibration of reference implants for Mg, Ca, Cr: Glass parameters and the calibrated implant fluence

Standard glass parameters				Implant				
	Type	Density (g cm ⁻³)	Concentration (ppm)	Implanted isotope	Implant identification number	Nominal fluence (10 ¹³ cm ⁻²)	Mean calibrated fluence (10 ¹³ cm ⁻²)	Number (n) of analyses
Mg	NIST 617	2.51	26.5±0.4 ¹	²⁵ Mg	K SRINI 4 02/2010	3.0	2.73±0.08	7
Ca	SRM 93a	2.26	86.8±1.4	⁴² Ca	K Al,42Ca 04/2013	1.0	1.18±0.05	3
Cr	NIST 612	2.51	36.26±1.16 ²	⁵² Cr	CEI 62Ni,52Cr 01/2013	4.0	4.16±0.18	6

¹ Burnett et al. (2015)

² Jochum et al. (2011)

A4. Noble gas fluences in the solar wind derived from Genesis targets

The noble gas fluences shown in Table 1 in the main text are based on the values published by Heber et al. (2009; 2012) for He, Ne, and Ar and by Vogel et al. (2011; 2019) for Kr and Xe, with values for major isotopes of each element given in these publications being recalculated to elemental fluences using SW isotopic ratios measured in Genesis targets by Heber et al. (2009; 2012) for He, Ne, Ar and Meshik et al. (2014; 2020) for Kr and Xe (for the latter two elements Bulk SW isotopic composition was assumed also for the regimes). In detail, for He, Ne, and Ar we adopt values from the DOS targets analyzed by Heber et al. (2009; 2012) and fully published (including the DOS regime) in Table 2 in Vogel et al. (2019). For Bulk SW we adopt the data measured in the Bulk SW targets (as opposed to calculated values based on exposure weighed regime targets). The Kr and Xe fluences in Table 1 are based on the CZ-Si target analyses given by Vogel et al. (2019); again for Bulk SW we rely on the data from the Bulk SW Si target. Since the ^{36}Ar fluences measured in the different Si samples differ by up to 5% from the preferred DOS values, we adjusted the Kr and Xe fluences reported by Vogel et al. (2019) to account for these differences, i. e. we adopt the mean flux ratios Kr/Ar and Xe/Ar Bulk SW and each regime, respectively.

Table 7
Solar abundances used in this work

Element	FIP (eV)	abundance (dex)	\pm	Element/Mg	\pm^a	reference
C	11.26	8.43	0.05	6.76	0.81	1
N	14.53	7.83	0.05	1.70	0.24	1
O	13.61	8.69	0.05	12.3	1.5	1
Na	5.14	6.21	0.04	0.0417	0.0040	2
Mg	7.65	7.59	0.04	= 1		2
Al	5.99	6.43	0.04	0.0692	0.0036	2
K	4.34	5.04	0.05	0.0028	0.0003	2
Ca	6.11	6.32	0.03	0.0537	0.0038	2
Cr	6.77	5.62	0.04	0.0107	0.0010	3
Fe	7.87	7.47	0.04	0.759	0.072	3
H	13.6	12		25700	3080	
He ^b	24.58	10.92	0.01	2140	105	4
Ne ^c	21.56	8.05	0.02	2.87	0.12	5
Ar ^c	15.75	6.36	0.04	5.87E-2	0.50E-2	5
Kr ^d	13.99	3.25		4.56E-5	0.33E-5	
Xe ^e	12.13	2.26		4.66E-6	0.29E-7	

Notes.

^a not including Mg uncertainty.

^b Helioseismology

^c Ne/He & Ar/He vs. H/He in Genesis regimes extrapolated to solar H/He according to Huss et al. (2020) with slightly updated Ne & Ar values obtained with data in Table 1 of this work.

^dinterpolated from CI chondrite abundances of neighboring elements.

^e from s-process σ_n trends.

References. (1) Asplund et al. (2009). (2) Scott et al. (2015a). (3) Scott et al. (2015b). (4) Basu & Antia (2008) (5) Huss et al. (2020)

Table 8
Fluence ratios (Element/Mg) in solar wind regimes normalized to solar values:
 $(E/Mg)_{SW}/(E/Mg)_{sol}$

	Bulk SW	±	Slow	±	Fast	±	CME	±
C	0.536	0.074						
N	0.409	0.073						
O	0.537	0.087						
Na	1.706	0.205	1.728	0.033	1.672	0.085	1.710	0.047
Mg	1.000	0.107	1.000	0.019	1.000	0.023	1.000	0.015
Al	1.186	0.174	1.114	0.048	1.107	0.030	1.205	0.048
Ca	1.259	0.118	1.243	0.013	1.232	0.019	1.352	0.008
Cr	1.252	0.140						
H	0.367	0.059	0.338	0.012	0.445	0.005	0.352	0.013
He	0.227	0.014	0.208	0.001	0.255	0.001	0.263	0.001
Ne	0.266	0.036	0.249	0.001	0.312	0.001	0.287	0.001
Ar	0.333	0.057	0.315	0.002	0.404	0.004	0.330	0.002
Kr	0.279	0.030	0.264	0.003	0.340	0.006	0.271	0.003
Xe	0.604	0.064	0.546	0.012	0.619	0.027	0.560	0.028

Fluence ratios shown in Fig. 2

A5. Comparison of Genesis and *in-situ* inter-regime element ratios

As discussed in conjunction with Figure 2b and Table 2 in the text, our results show very similar element/Mg ratios among the three regimes at a very high level of precision for low FIP elements. Here we show that this result is compatible with previous studies of SW composition. *All abundance data in this section are the measured SW ratios, no data normalized to spectroscopic photospheric ratios are used.* Beyond the higher precision of our data, there are other reasons why the similarity in low FIP trends has not been recognized: (1) use of O normalization. (2) Differences (at present) among low FIP elements for Genesis and spacecraft instrument studies.

O normalization. Discussions of SW composition require a reference element. O is the logical choice for spacecraft data, as the data are very precise. All spacecraft data papers, except Pilleri et al. (2015), normalize to O. For Genesis, O is difficult to measure, in contrast to Mg, which we have adopted as a reference element. The widely-accepted qualitative interpretation of the large low - high FIP elemental fractionation in all coronal and solar particle abundance data is that it represents lack of complete ionization for high FIP elements, producing their depletion. Correct interpretations do not require any specific reference element; however, in terms of assessing inter-regime variations of low FIP elements, data normalized to a high FIP element (e.g. O) can be confusing. Using the most recent revised ACE SWICS data (Pilleri et al. 2015) for the Genesis mission period, the L ("Slow SW") and H ("Fast SW") Mg/O ratios are 0.156 and 0.128 respectively. Since the photospheric Mg/O is 0.079, one concludes, correctly, that the H SW is less fractionated. But, the statement: "L solar wind is more enhanced in low FIP elements than H solar wind", although numerically correct, is potentially misleading because the main fractionation is between low FIP elements as a group and *any* specific high FIP element. The cause of the (L,H) Mg/O difference is less O depletion in the H solar wind. This

is totally semantic, but O normalization makes the very similar inter-regime element ratios of low FIP elements more difficult to see. This problem does not arise in Mg-normalized data.

Element Selection. Our high precision inter-regime comparisons involve: Na, Ca, Al, and Mg. The most accurate ACE SWICS data (Pilleri et al. 2015) only have Mg, Fe and Si. The only overlap is Mg. With FIP = 8.15 eV, Si may not be a low FIP element; nevertheless, the L and H Si/Mg ratios are very close: 1.19 and 1.21. The spectroscopic photospheric ratio is 0.81 ± 0.11 (Asplund et al. 2009), possibly not significant relative to Pilleri at 2 sigma. The main point is that the Si/Mg is the same in L and H solar wind, consistent with the conclusion from our data for other low FIP elements. Pilleri et al., give evidence that a separate mass-dependent fractionation causes L-H differences in Fe/Mg.

Comparison with MTOF abundances. In order to deal with the complex SW charge state distribution, the Mass Time of Flight (MTOF) mass spectrometer (Hovestadt et al. 1995; Heidrich-Meisner et al. 2016) passed velocity-selected SW ions through a thin foil such that only +1 charged ions emerged. Beautiful mass spectra were obtained, but there have been major problems in obtaining quantitative elemental abundances because a large correction is required for the fraction of incoming ions that emerge from the foil as neutrals. Progress appears to have been made (Heidrich-Meisner et al. 2016) by intercalibration with SWICS, but quantitative abundances are not yet available. A full set of MTOF abundances for the same elements as measured here is available in Table 1 of Bochsler (2009). For L and H SW; the Na/Mg, Al/Mg, and Ca/Mg ratios are the same in L and H solar wind, although the errors range from 25 to 75%, compared to our 2-5%.